ACS APPLIED POLYMER MATERIALS

pubs.acs.org/acsapm

Article

Nitrogen- and Sulfur-Rich Microporous Carbons Derived from Conjugated Microporous Polymers for CO_2 Uptake, Supercapacitor Energy Storage, and Electrochemical Hydrogen Production

Poonam Nagendra Singh,[▽] Mohamed Gamal Mohamed,[▽] Mohammed G. Kotp, Tapomay Mondal, Swetha V. Chaganti, Mervat Ibrahim, Santosh U. Sharma, Yunsheng Ye, and Shiao-Wei Kuo*

Cite This: ACS Appl. Polym. Mater. 2025, 7, 3324−3336

Read Online

ACCESS | Metrics & More | Article Recommendations | Supporting Information

ABSTRACT: In this work, we synthesized Py-DPABT CMP through Sonogashira−Hagihara cross-coupling reactions between N^4,N^7-bis(4-bromophenyl)-N^4,N^7-diphenylbenzo[*c*][1,2,5]-thiadiazole-4,7-diamine (DPABT-Br_2) and 1,3,6,8-tetraethynylpyrene (Py-T). This Py-DPABT CMP was subsequently carbonized at 500 and 700 °C and transformed into a porous carbonaceous electrode precursor for supercapacitors (SCs), yielding Py-DPABT CMP-500 and Py-DPABT CMP-700 containing N and S heteroatoms. Using distinct analytical methods, we investigated the electrochemical characteristics, CO_2 uptake, configuration, porosity, thermal stability, and chemical structure of the Py-DPABT CMP before and after carbonization at 500 and 700 °C, respectively. After carbonization, the material (Py-DPABT CMP-500) achieved a BET surface area (SA_{BET}) of 423 m^2 g^{-1} and the adsorption capacity of CO_2 reached 3.55 mmol g^{-1} at 0 °C. Electrochemical evaluations revealed that Py-DPABT CMP-500 exhibited enhanced performance when utilized as supercapacitor electrodes, facilitated by heteroatoms. According to three-electrode analyses, Py-DPABT CMP-500 achieved specific capacitances up to 973 F g^{-1} at 1 A g^{-1}. Additionally, they demonstrated exceptional durability, maintaining 98% of their capacity after 2000 cycles when tested at a current of 10 A g^{-1}. Furthermore, the capacitance of the symmetric coin cell Py-DPABT CMP-500 at 1 A g^{-1} achieved 627 F g^{-1}. The hydrogen evolution reaction and performance of Py-DPABT CMP-500 were assessed in 1 M KOH electrolyte utilizing a three-electrode setup. The catalyst achieved a current density of 10 mA cm^{-2} with an overpotential of 325 mV and exhibited a Tafel slope of 169 mV dec^{-1}. Additionally, it demonstrated a low charge transfer resistance (R_{ct}) of 88 Ω and a substantial double-layer capacitance (C_{dl}) of 72.8 mF cm^{-2}, highlighting its potential as an efficient electrocatalyst for HER applications. These findings underscore the potential practical applications of this electrode and investigate the synergistic effects of heteroatoms and the carbonization process in CMPs, enhancing their suitability for CO_2 uptake, supercapacitor, and HER.

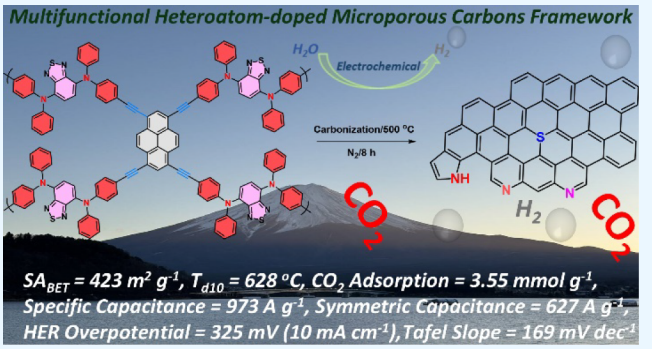

KEYWORDS: *pyrene, benzo[c][1,2,5]thiadiazole, conjugated microporous polymers, heteroatom-doped microporous carbons, CO_2 uptake, supercapacitors*

INTRODUCTION

The growing adoption of renewable energy sources and the need for low-emission transportation have reignited interest in energy storage, acknowledged as a key element of sustainable development.[1−5] Energy preservation is very important in renewable energy systems.[1−5] To address the demands of modern society and increasing environmental concerns, it is crucial to develop new, accessible, and ecofriendly energy storage methods. Given their fast charging and discharging functions, durability, and positive environmental impact, supercapacitors (SCs), also known as electrochemical capacitors (ECs), are increasingly considered to be among the most viable alternatives to storing energy.[6−10] Supercapacitors (SCs) stand out because their energy density far surpasses that of traditional dielectric capacitors by several orders of magnitude. SCs utilize two principal mechanisms for energy storage: Faradaic pseudocapacitance, which relies on reversible redox reactions within the electrode materials, and non-Faradaic electrochemical double-layer capacitance (EDLC) processes.[6−10] While pseudocapacitors offer higher capacitance than most EDLCs because of redox processes that

Received: January 2, 2025
Revised: February 18, 2025
Accepted: February 18, 2025
Published: February 23, 2025

can be reversed at the electrode surface, EDLCs achieve charge storage through ion adsorption at the electrode−electrolyte interface.[11−13] Both types of capacitors require electrode materials with a high specific surface area to function effectively.[14] Issues related to the environment have increasingly become a focal point for researchers, especially with the onset of the modern industrial revolution and the pressing challenge of global warming.[15,16] The primary contributors to global warming are greenhouse gas emissions, including CO_2, N_2O, and CH_4.[17] Among these, CO_2 is often considered the principal culprit behind global warming and climate change, with its atmospheric concentration growing.[18,19] In 2021, atmospheric carbon dioxide levels reached a record high of 419 ppm, leading to significant environmental impacts.[20] Therefore, reducing and managing carbon emissions is a critical global issue. CMPs are constructed by linking rigid, π-conjugated building blocks incorporating various functionalities, forming three-dimensional macromolecular networks characterized by micropores (<2 nm) and extensive permanent surface areas.[21−24] Unlike linear polymers, the porous structure of CMPs significantly enhances electron/ion transport. Typically, CMPs are synthesized using C−C coupling reactions, similar to those used for linear conjugated polymers, such as Suzuki, Sonogashira, and Yamamoto coupling, or through chemical oxidative polymerization.[25−27] These methods facilitate high levels of polymerization and cross-linking, allowing the integration of diverse organic groups. CMPs are promising for applications in energy storage, gas storage, and catalysis due to their network structure. Conjugated polymers are crucial in various electrical devices due to their ability to interact with light and conduct charge carriers, and they offer extensive possibilities for molecular and supramolecular engineering.[28−30] By choosing appropriate repeating units, these polymers can be made electron-rich or electron-deficient, enabling the stabilization of holes or electrons and allowing precise control over their band gaps to alter absorption and emission wavelengths. On a supramolecular level, solid-state packing can be finely adjusted to achieve high charge-carrier mobilities. Unfortunately, the poor electrical conductivity and limited chemical and oxidative durability of CMPs make them unsuitable for electrode applications. However, several approaches have been suggested to improve the capacitance of CMPs, including increasing their electrical conductivity through carbonization, hybridization with nanomaterials, or structural modification. Physical or chemical activation is commonly required in the broader carbon materials field to enhance the pore network development. Pyrolysis is frequently employed to produce porous carbon materials from biomass, and activation techniques improve specific surface area (SSA) and pore volume.[31] There has been growing interest in donor−acceptor (D-A) polymers, characterized by an alternating sequence of donor and acceptor units.[32] This configuration is ideal for creating small band gap-conjugated polymers, as the redox properties of the donor and acceptor units can be chemically tailored. Research has included various groups of donors, acceptors, and π-bridges.[33,34] For instance, donor−acceptor electron pairs are often formed by groups such as diphenylamine (DPA), carbazole, and benzothiadiazole (BT), with π-bridges typically comprising benzene and thiophene rings.[33] BT is particularly prevalent in organic electronics as an acceptor heterocycle.[34,35] BT rings featuring identical substituents at positions 4 and 7 are described as identical configurations. These structures are commonly used as monomers for crafting donor−acceptor polymers and creating small molecules with extensive optoelectronic properties.[36,37] Diphenylamine (DPA) is favored in optoelectronics for its robust electron-donating ability, which can be attributed to the lone pair of electrons. Its rigid structure enhances solubility in organic solvents and provides thermal stability.[38,39] In various studies, DPA serves as an electron donor paired with different electron acceptors, resulting in structures with nonlinear optical properties, such as fluorescence. Due to its significance in electron transport, DPA is a valuable component in developing optoelectronic materials.[40,41] Several porous carbon materials can be used for both CO_2 capture and supercapacitor applications. For instance, Hu et al. reported that SPC-900 exhibited a particular capacity of 363 F g^{-1}.[42] Our study showed that the RES-HP-BZ-800 polymer exhibited a capacitance of 523 F g^{-1} and captured CO_2 at a rate of 4.63 mmol g^{-1} at 298 K.[43] This research generated and prepared heteroatom-rich microporous carbons using Sonogashira coupling between DPABT-Br_2 and Py-T to produce Py-DPABT CMP and carbonized Py-DPABT CMP at 500 and 700 °C. Various characterization techniques were employed to investigate how different technical parameters influence the morphology and pore structure of the Py-DPABT CMP, Py-DPABT CMP-500, and Py-DPABT CMP-700. Additionally, CO_2 adsorption and electrochemical experiments were conducted to explore the relationship between the pore structure and electrochemical properties. Notably, Py-DPABT CMP-500 demonstrated excellent CO_2 capture, rate performance, and cycle stability in a three-electrode symmetric coin cell system. It achieved a capacitance of up to 973 F g^{-1}. The HER was also carried out in 1 M KOH electrolytes of Py-DPABT CMP-500 in a three-electrode setup. To obtain a current density of 10 mA cm^{-2}, Py-DPABT CMP-500 required a 325 mV overpotential. Additionally, Py-DPABT CMP-500 was a considerable electrocatalyst for HER application because of its low R_{ct} value of 88 Ω and noteworthy C_{dl} value of 72.8 mF cm^{-2}.

EXPERIMENTAL SECTION

Materials. Benzo[*c*][1,2,5]thiadiazole (BT), diphenylamine (DPA), palladium(II) acetate [$Pd(OAc)_2$], tri*tert*-butyl phosphine tetrafluoroborate ($C_{12}H_{27}BF_4P$), sodium *tert*-butoxide (NaOtBu), toluene, dichloromethane (DCM), anhydrous Na_2SO_4, hexane, potassium carbonate (K_2CO_3), *N*-bromosuccinimide (NBS), copper(I) iodide (CuI), triphenylphosphine (PPh_3), and $Pd(PPh_3)_4$. The BT-Br_2 and Py-T were prepared according to our published methods.[44−47] The FTIR spectrum of the Py-T monomer (Figure S1) displayed characteristic absorption bands at 3278, 3042, and 2090 cm^{-2}, which correspond to the stretching vibrations of alkyne C−H, aromatic C−H, and the —C≡C triple bond, respectively.[44,45]

Preparation of N^4,N^4,N^7,N^7-tetraphenylbenzo[*c*][1,2,5]-thiadiazole-4,7-diamine [DPABT]. We combined and dissolved NaOtBu (2.85 g, 29.6 mmol), $Pd(OAc)_2$ (121 mg), BT-Br_2 (3.95 g, 13.45 mmol), DPA (5 g, 29.6 mmol), and $C_{12}H_{27}BF_4P$ (0.47 mg, 1.61 mmol) in 180 mL of dry toluene under an argon atmosphere. We agitated the solution at its boiling point for 24 h and then allowed it to cool to ambient temperature. Subsequently, the reaction mixture was gradually transferred into water and subjected to extraction using DCM. We dehydrated the organic phase using anhydrous Na_2SO_4, separated it by filtration, and concentrated it by reducing the pressure. Column chromatography refined the raw product using a mixture of DCM and hexane in a volume ratio of 2:1 as the solvent. Ultimately, we obtained the orange powder DPABT in a substantial yield of up to 85% (5.1 g).

Preparation of N^4,N^7-bis(4-bromophenyl)-N^4,N^7-diphenylbenzo[*c*][1,2,5]thiadiazole-4,7-diamine [DPABT-Br_2].

https://doi.org/10.1021/acsapm.5c00012
ACS Appl. Polym. Mater. 2025, 7, 3324−3336

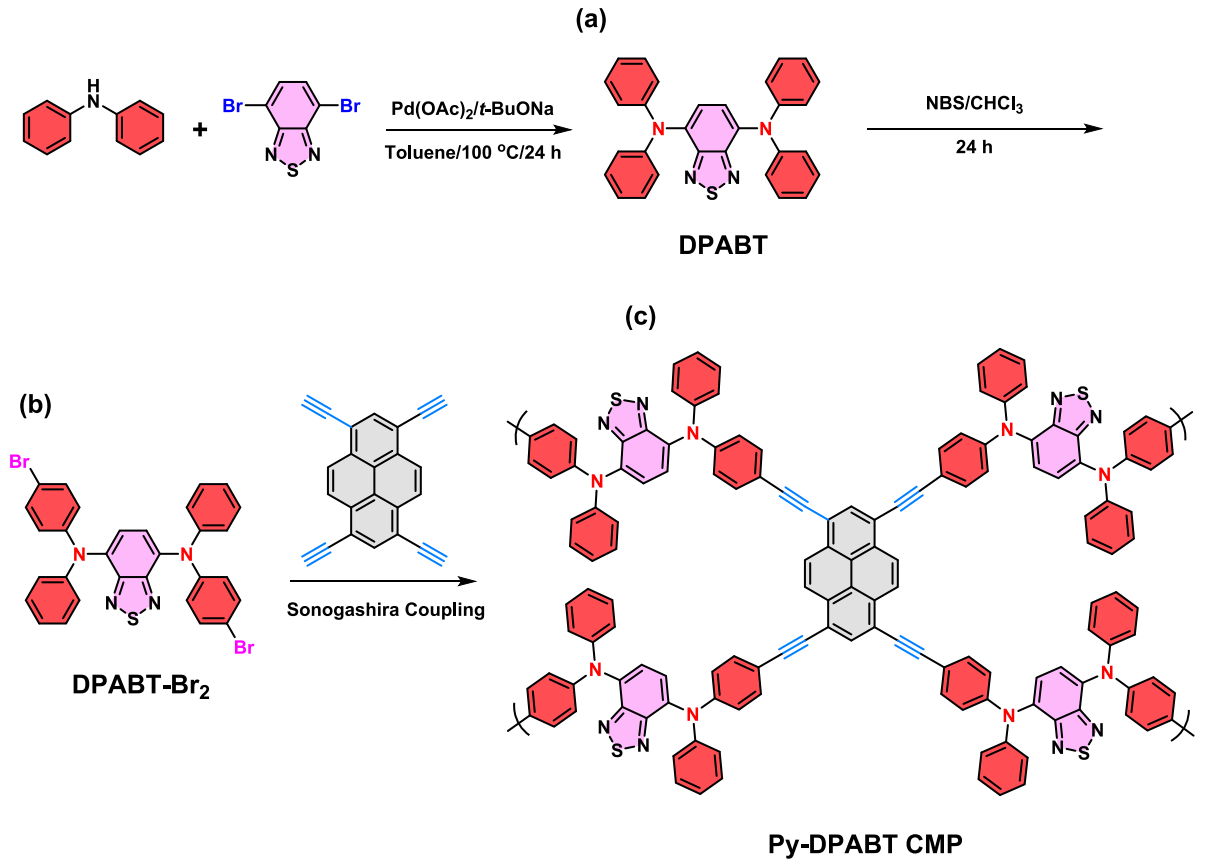

Figure 1. Synthesis of (a) DPABT, (b) DPABT-Br_2, and (c) Py-DPABT CMP.

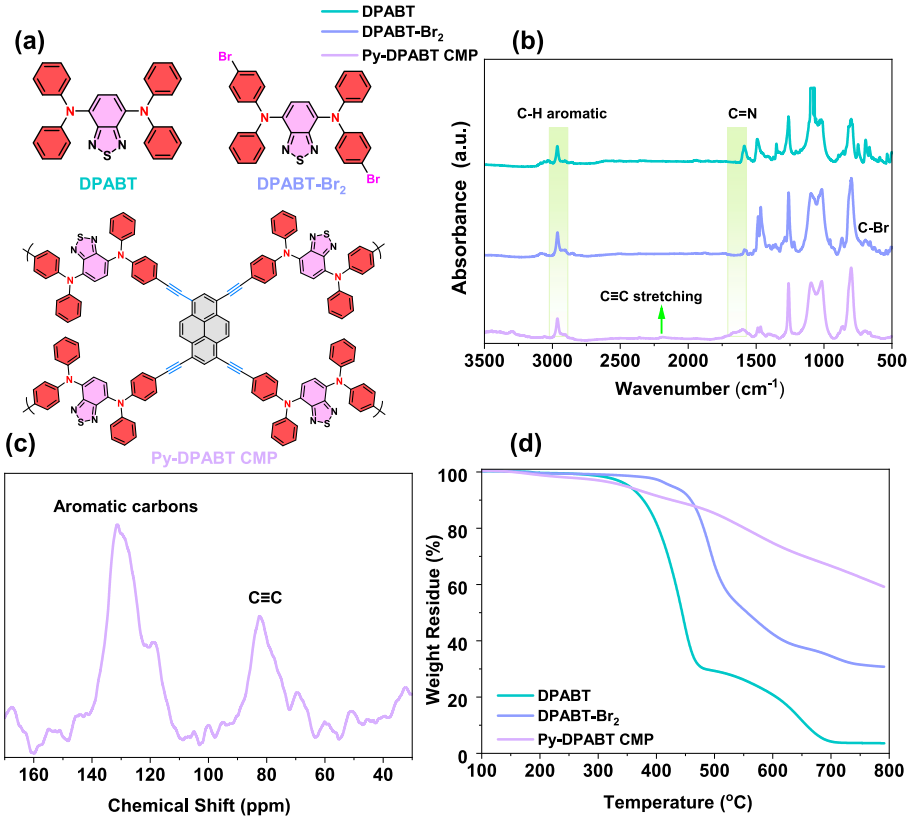

Figure 2. (a) Chemical structures, (b) FTIR, of DPABT, DPABT-Br_2, and Py-DPABT CMP, (c) solid-state ^{13}C NMR of Py-DPABT CMP, and (d) TGA analyses of DPABT, DPABT-Br_2, and Py-DPABT CMP.

https://doi.org/10.1021/acsapm.5c00012
ACS Appl. Polym. Mater. 2025, 7, 3324−3336

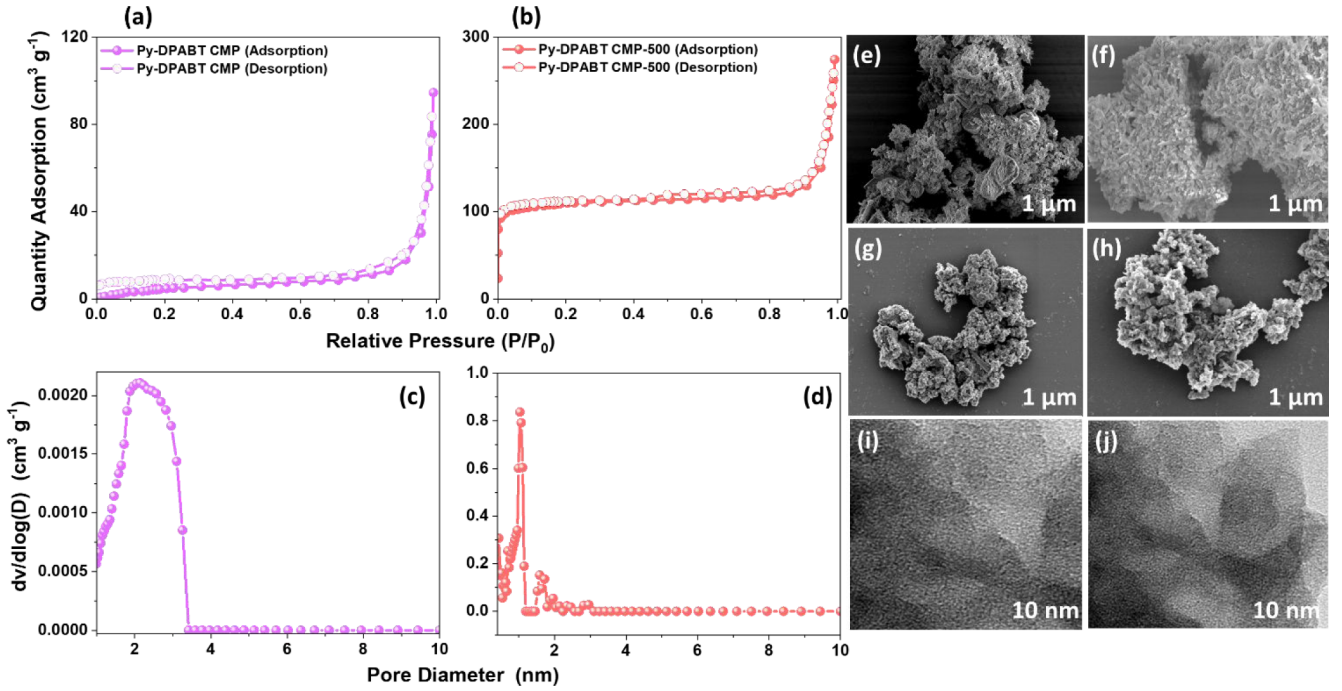

Figure 3. (a, b) N_2 adsorption−desorption and (c, d) pore size profiles, (e, h) SEM, and (i, j) TEM images of (a, c, e, f, i) Py-DPABT CMP and (b, d, g, h, j) Py-DPABT CMP-500.

A mixture contained 3 g (4.8 mmol) of DPABT and 6.8 g (38.2 mmol) of NBS in 30 mL of $CHCl_3$. The mixture was agitated at 0 °C and left in the dark at room temperature for 12 h. Subsequently, the organic solvent was removed, and the pure DPABT-Br_2 was obtained using silica column chromatography with a mixture of DCM and hexane in a volume ratio of 2:1 as the solvent. Eventually, the resulting substance produced was in the form of an orange powder.

Preparation of Py-DPABT CMP. The preparation of Py-DPABT CMP as a dark brown powder was performed by heating a mixture of DMF (25 mL) and Et_3N (25 mL) with CuI (20 mg), Py-T (500 mg, 1.67 mmol), DPABT-Br_2 (2.11 mg, 3.36 mmol), PPh_3 (26 mg), and $Pd(PPh_3)_4$ (116 mg) at 110 °C for about 2−3 days. After that, the insoluble material was repeatedly cleaned using acetone and MeOH through Soxhlet extraction, and the resulting powder was dried at 120 °C.

Preparation of Py-DPABT CMP-500 and Py-DPABT CMP-700. We carbonized the Py-DPABT CMP sample for 8 h at 500 and 700 °C, with an increasing temperature of 5 °C min^{-1}, influenced by N_2 gas. The carbonized material produced was known as Py-DPABT CMP-500 and Py-DPABT CMP-700 (Scheme S1).

RESULTS AND DISCUSSION

Synthesis and Characterization of Py-DPABT CMP, Py-DPABT CMP-500, and Py-DPABT CMP-700. In this study, we combined BT-Br_2, DPA, NaOtBu, $Pd(OAc)_2$, and $C_{12}H_{27}BF_4P$ in dry toluene and allowed the mixture to reflux to afford an orange solid monomer DPABT (Figure 1a). This was followed by a 12-h reaction of the DPABT monomer with NBS in $CHCl_3$, producing the orange solid DPABT-Br_2 (Figure 1b). Finally, a Sonogashira coupling reaction over 3 days between DPABT-Br_2 and Py-T monomers yielded the dark brown solid, Py-DPABT CMP (Figure 1c). Initially, we employed ^1H and ^{13}C NMR spectroscopy to verify the synthesis of DPABT and DPABT-Br_2, as illustrated in Figures S2−S5. Figures S2 and S4 show the aromatic CH peaks at 7.26 and 6.98 ppm for DPABT, respectively, and at 7.52, 7.37, 7.11, 6.99, 6.9, and 6.75 ppm for DPABT-Br_2. The aromatic carbon resonance signals for DPABT (Figure S3) were observed at 152.99, 148.02, 136.04, 130.07, 126.57, and 123.58 ppm. For DPABT-Br_2, these signals appeared in the range from 153.81 to 121.39 ppm (Figure S5). Figure 2a−d presents the chemical structures and structural analysis of DPABT, DPABT-Br_2, and Py-DPABT CMP using FTIR, ^{13}C SSNMR, and TGA techniques. Figure 2b illustrates FTIR spectra of Py-DPABT CMP at room temperature, showing absorption peaks at 1266, 1590, 1490, and 3043 cm^{-1}, correlated to the C−N, C═N, C═C, and CH aromatic units, respectively. An additional apex at 2194 cm^{-1}, indicative of the —C≡C group, suggests the successful formation of cross-linked networks between DPABT-Br_2 and Py-T. The FTIR spectra for DPABT and DPABT-Br_2 revealed similar peaks, such as aromatic CH, C═N, and C═C units, akin to those observed in Py-DPABT CMP. Additionally, DPABT-Br_2 exhibited an extra peak at 691 cm^{-1}, which is associated with C−Br bonding, as illustrated in Figure 2b. Solid-state ^{13}C NMR analysis (Figure 2c) revealed more details about the chemical structure of Py-DPABT CMP. It identified the presence of aromatic carbon and C−N resonances between 145.47 and 117.89 ppm and also detected both terminal and internal alkyne carbon units at 82.49 ppm. These findings confirm the effectiveness of the Sonogashira-Hagihara coupling. TGA analysis was performed on Py-DPABT CMP and its components [DPABT and DPABT-Br_2] in a nitrogen atmosphere (Figure 2d) to assess their thermal stability. Py-DPABT CMP demonstrated superior thermal stability compared to those of DPABT and DPABT-Br_2. It reached a thermal decomposition temperature at a 10% weight loss of 428 °C and achieved a char yield of 59 wt %. By comparison, DPABT decomposed at 387 °C with a char yield of 3.59 wt %, while DPABT-Br_2 showed decomposition at 459 °C and a char residue of 30.78 wt %. Scheme S1 depicts the probable chemical structure of Py-DPABT CMP following carbonization at 500 and 700 °C in a nitrogen atmosphere to afford Py-DPABT CMP-500 and Py-DPABT CMP-700, respectively.

https://doi.org/10.1021/acsapm.5c00012
ACS Appl. Polym. Mater. 2025, 7, 3324−3336

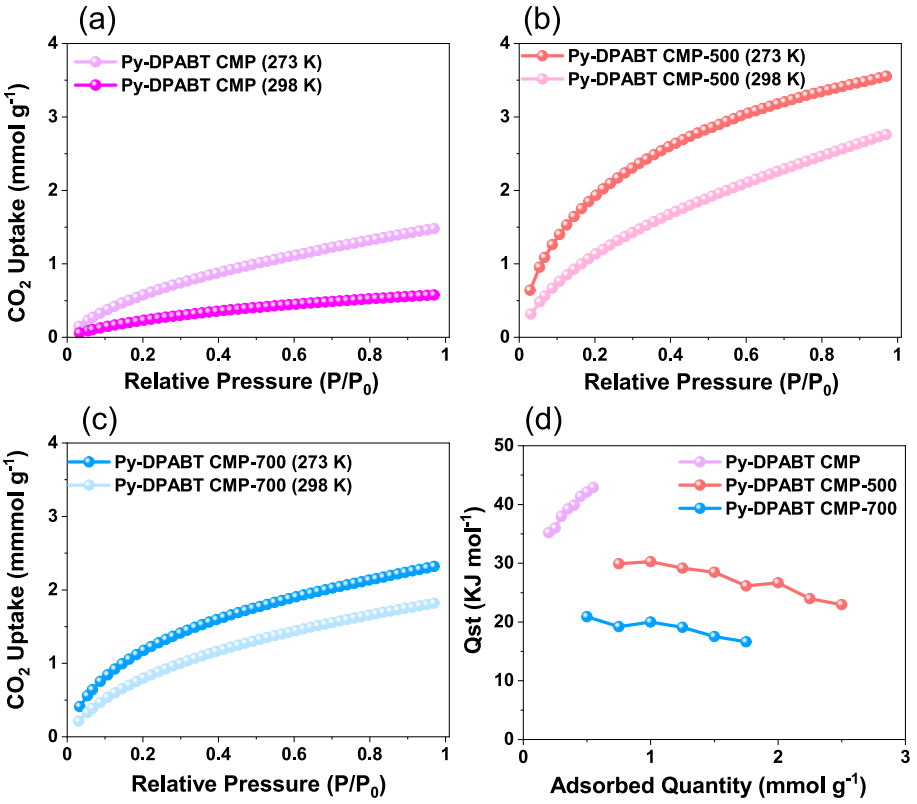

Figure 4. CO_2 uptake of (a) Py-DPABT CMP, (b) Py-DPABT CMP-500, and (c) Py-DPABT CMP-700 were recorded at 25 and 0 °C, and (d) Q_{st} profile of Py-DPABT CMP, Py-DPABT CMP-500, and Py-DPABT CMP-700.

XRD analysis confirmed the amorphous nature of Py-DPABT CMP (Figure S6). The Py-DPABT CMP-500 and Py-DPABT CMP-700 exhibited a T_{d10} up to 629 and 678 °C, respectively, with a char yield of 83.4 and 81.1 wt % as shown in Figure S7. The phase structure and vibrational properties of Py-DPABT CMP-500 were investigated using Raman spectra and X-ray diffraction (XRD) patterns. These methods provided comprehensive insights into the material's crystalline structure and molecular vibrations, which are essential for understanding its physical properties and potential applications. XRD analysis revealed two peaks at a 2θ value of 23.1° and 43°, corresponding to the (002) plane and (101) planes (Figure S8), suggesting the existence of ordered hexagonal carbon and a graphitized structure.[48,49] These observations confirm the successful transformation of the Py-DPABT CMP into the intended microporous carbons with heteroatoms, including N and S, leading to disordered amorphous carbon structures in Py-DPABT CMP-500, which exhibit excellent porosity and energy storage capabilities. Raman spectroscopy of Py-DPABT CMP-500 and Py-DPABT CMP-700 (Figure S9) showed two different groups: the G group at 1592 cm^{-1} and the D group at 1326 cm^{-1}.[50] ID/IG was determined to be 2.83 and 1.33 for Py-DPABT CMP-500 and Py-DPABT CMP-700, respectively. To study the distribution of carbon, nitrogen, as well as sulfur atoms on the surface of Py-DPABT CMP-500, we performed an XPS investigation (Figure S10a–d). The C 1s spectrum of Py-DPABT CMP-500 exhibits two distinct peaks: one at 284.8 eV correlates to aromatic sp^2 carbon and the second at 286.4 eV, assigned to the C═N bond (Figure S10b). In the N 1s profile (Figure S10c), peaks at 399.5 and 400.5 eV are observed, corresponding to C═N and N–S bonds, respectively.[51] Additionally, the S2p spectrum (Figure S10d) shows peaks at 156.03 and 158.53 eV, representing the S2p3/2 and S 2p1/2, respectively. To evaluate the porosity and surface area characteristics of Py-DPABT CMP, Py-DPABT CMP-500, and Py-DPABT CMP-700 at 77 K, nitrogen adsorption and desorption tests were conducted, as depicted in Figures 3a–d and Figure S11. Py-DPABT CMP displayed type III isotherms according to Figure 3a, while Py-DPABT CMP-500 and Py-DPABT CMP-700 showed type I adsorption–desorption isotherms, as indicated in Figures 3b and S11a.

The rapid nitrogen adsorption at low pressures in Py-DPABT CMP-500 and Py-DPABT CMP-700 indicated a high number of micropores. The SA_{BET} as well as the overall volume of pores (V_{total}) of the Py-DPABT CMP were measured at 25 $m^2\ g^{-1}$ and 0.14 $cm^3\ g^{-1}$. In contrast, Py-DPABT CMP-500 and Py-DPABT CMP-700 showed significantly higher values of 423 and 203 $m^2\ g^{-1}$ for SA_{BET} and 0.4091 and 0.15 $cm^3\ g^{-1}$ for V_{total}. Pyrolyzing Py-DPABT CMP at 500 °C resulted in a substantial increase in nitrogen uptake and a more porous structure, enhancing pore formation in Py-DPABT CMP-500.[52] Further analysis using nonlocal density functional theory (NLDFT) explored how pore sizes were distributed in both Py-DPABT CMP, Py-DPABT CMP-500, and Py-DPABT CMP-700, as shown in Figures 3c,d and S11b. The results revealed that the Py-DPABT CMP exhibits a peak at 2.11 nm. In contrast, Py-DPABT CMP-500 shows a prominent peak at 1.02 nm along with additional peaks at 1.55 and 2.91 nm. Meanwhile, Py-DPABT CMP-700 features a major peak at 0.69 nm, with other peaks appearing at 1.22 and 1.55 nm, underscoring its microporous structure. Scanning electron microscopy and transmission electron microscopy were used to evaluate the morphology and structure of Py-DPABT CMP

https://doi.org/10.1021/acsapm.5c00012
ACS Appl. Polym. Mater. 2025, 7, 3324–3336

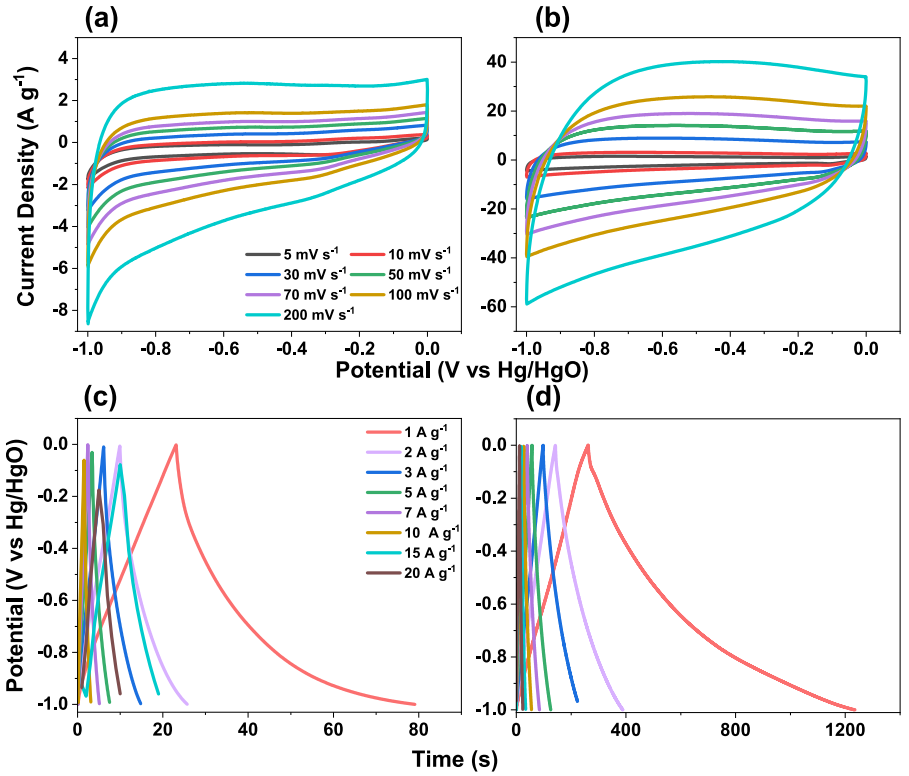

Figure 5. (a, b) CV and (c, d) GCD profiles of (a, c) Py-DPABT CMP and (b, d) Py-DPABT CMP-500.

and its calcined variants, Py-DPABT CMP-500 and Py-DPABT CMP-700, as illustrated in Figures 3e–j and S12. SEM images showed that the Py-DPABT CMP consists of clusters of aggregated nanoparticles (Figures 3e,f and S12a–c). Py-DPABT CMP-500, on the other hand, displayed spherical particles with a uniform distribution of pores, as evident in Figures 3g,h and S12d–f. Furthermore, Py-DPABT CMP-700 exhibited spherical particles combined with a nanorod structure, as shown in Figure S12g–i. This indicates that the carbonization process contributes to increased porosity and uniformity of the structural properties of the material. For instance, the TEM analysis depicted in Figure 3i,j revealed that both Py-DPABT CMP and Py-DPABT CMP-500 exhibited interconnected microporous structures typical of amorphous porous materials. SEM-EDS images (Figure S13a–c) verified the uniform distribution of C, nitrogen, N, and S within the matrices of Py-DPABT CMP, Py-DPABT CMP-500, and Py-DPABT CMP-700. The CO_2 uptake measurements provide valuable insights into the adsorption properties of these materials. The pristine Py-DPABT CMP exhibited a CO_2 uptake of 1.5 mmol g^{-1} at 273 K and 0.6 mmol g^{-1} at 298 K (Figure 4a), reflecting a moderate capacity for gas adsorption. Upon carbonization at 500 °C, the level of CO_2 uptake significantly increased to 3.6 mmol g^{-1} at 273 K and 2.8 mmol g^{-1} at 298 K (Figure 4b). This marked enhancement in CO_2 uptake is attributed to the increased porosity and surface area of Py-DPABT CMP-500, which achieved a surface area of 423 m^2 g^{-1}. The increase in surface area plays a critical role by providing enhanced active areas for gas molecule adsorption, therefore enhancing the whole adsorption performance of the material.[53−55] Conversely, carbonization at 700 °C yielded a CO_2 uptake of 2.31 mmol g^{-1} at 273 K and 1.81 mmol g^{-1} at 298 K (Figure 4c) for Py-DPABT CMP-700.

This reduction in CO_2 uptake is accompanied by a lower surface area of 203 m^2 g^{-1}, indicating that higher carbonization temperatures may result in structural collapse or decreased porosity. Such an effect is likely due to the excessive carbonization process, which can lead to degradation of the porous framework, thereby diminishing the available surface area for gas adsorption. These findings suggest that while moderate carbonization can enhance gas uptake through increased surface area, higher temperatures may have a detrimental impact, leading to a reduction in the adsorption capacity. The pristine Py-DPABT CMP displays relatively high Q_{st} values, ranging from 35.21 to 42.9 kJ mol^{-1} (Figure 4d), as the CO_2 uptake increases from 0.2 to 0.55 mmol g^{-1} (Figure 4d). These high Q_{st} values indicate that the initial adsorption sites on the material surfaces are energetically favorable for CO_2 capture, likely due to the presence of specific functional groups or pore structures that facilitate strong interactions with the CO_2 molecules. In contrast, Py-DPABT CMP-500 exhibits lower Q_{st} values, ranging from 22.96 to 30.28 kJ mol^{-1}, as the amount of adsorbed CO_2 rises from 0.75 to 2.5 mmol g^{-1} (Figure 4d). This reduction in Q_{st} can be attributed to changes in the surface chemistry and pore architecture induced by the carbonization process. Carbonization at 500 °C likely modified the functional groups and produced a more uniform pore structure, resulting in a more homogeneous adsorption process with less variation in adsorption energetics. The overall decrease in Q_{st} values suggests that the interactions between CO_2 and the surface of Py-DPABT CMP-500 are weaker compared to those of the pristine material. This reduced interaction strength could be beneficial for the desorption of CO_2 and the regeneration of the adsorbent, enhancing its practical utility. Py-DPABT CMP, carbonized at 700 °C, demonstrates the lowest Q_{st} values among the three materials, ranging from 16.62 to 20.88 kJ mol^{-1} as the CO_2 uptake

https://doi.org/10.1021/acsapm.5c00012
ACS Appl. Polym. Mater. 2025, 7, 3324−3336

increases from 0.5 to 1.75 mmol g^{-1} (Figure 4d). This further reduction in Q_{st} compared to Py-DPABT CMP-500 is likely due to the more extensive carbonization at higher temperatures. Carbonization at 700 °C may have promoted the formation of a more graphitic structure with fewer functional groups, resulting in weaker interactions with the CO_2 molecules. The lower Q_{st} values indicate a less exothermic adsorption process, which could offer advantages in terms of reducing the energy required for CO_2 desorption, thereby improving the efficiency of the adsorption−desorption cycle.

Electrochemical Performance of Py-DPABT CMP, Py-DPABT CMP-500, and Py-DPABT CMP-700 Based on Three-Electrode System. We employed cyclic voltammetry (CV) and galvanostatic charge−discharge (GCD) measurements with a three-electrode setup to examine the electrochemical properties in 1 M KOH. The CV profiles for Py-DPABT CMP, Py-DPABT CMP-500, and Py-DPABT CMP-700 are shown in Figures 5a,b and S14a. Within a potential window from −1 to 0.0 V (vs Hg/HgO), the Py-DPABT CMP exhibited CV curves with different scan rates ranging from 5 to 200 mV s^{-1}. Usually, these curves showed a characteristic, humped shape that resembled a rectangle;[56−59] however, a peak at approximately −0.3 V diminished as the scan rate increased, indicating instability of Py-DPABT CMP under these conditions, as shown in Figure 5a. In contrast, Py-DPABT CMP-500 and Py-DPABT CMP-700 were evaluated under similar conditions, as shown in Figures 5b and S14a. This material maintained the characteristic rectangular humped profile consistently across all scan rates, suggesting stable electrochemical performance. This stability and pronounced capacitance behavior are attributed to the significant increase in surface area postcarbonization, electron-rich phenyl groups, an abundance of heteroatoms, and thermal activation, which collectively enhance performance across various scan rates. The aforementioned factors also enhance pseudocapacitance by facilitating efficient electron transfer through improved electrolyte contact.[43] We observe a bent triangular shape for Py-DPABT CMP, Py-DPABT CMP-500, and Py-DPABT CMP-700 when we focus on the GCD curves in Figures 5c,d and S14b, obtained at 1−20 A g^{-1}. This shape verifies the presence of EDLC and pseudocapacitance.[60−66]

The capacitance values measured up to 20 A g^{-1} are shown in Figure 6. Despite the initial high numbers of capacitance of 57, 973, and 230 F g^{-1} at 1 A g^{-1} for the Py-DPABT CMP, Py-DPABT CMP-500, and Py-DPABT CMP-700, respectively, as the current density increased, both materials' specific capacitance quickly dropped. This reduction in capacitance at higher current densities suggests that in Py-DPABT CMP, charge storage primarily occurs on the external active surface, as the electrolyte ions struggle to permeate through the internal pores at increased current rates. The significant improvement in capacitance observed in the Py-DPABT CMP-500 and Py-DPABT CMP-700 frameworks over the Py-DPABT CMP can primarily be attributed to the graphitic structure and heteroatoms. The formation of heteroatom-doped porous carbon not only increases the overall capacitance of the framework but also introduces additional charge storage sites in Py-DPABT CMP-500 compared to Py-DPABT CMP-700.[43,60−62] Owing to its vast surface area, enhanced conductivity, and ability to form double-layer capacitors, porous carbon possesses distinctive properties that contribute to this heightened capacitance. Consequently, the capacitance

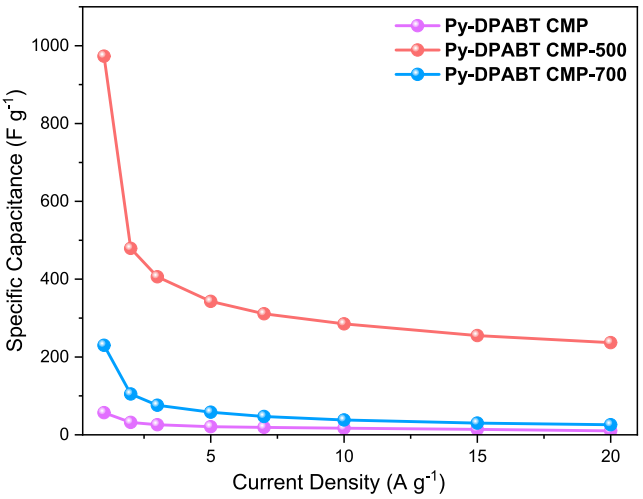

Figure 6. Specific capacitance values for Py-DPABT CMP, Py-DPABT CMP-500, and Py-DPABT CMP-700.

performance of Py-DPABT CMP-500 surpasses that of the Py-DPABT CMP and Py-DPABT CMP-700. Table S1 indicates that our Py-DPABT CMP-500 is a competitive option for supercapacitor electrodes compared with other electrode materials. Additionally, the capacitance retention of the Py-DPABT CMP, Py-DPABT CMP-500, and Py-DPABT CMP-700 was evaluated by subjecting them to 5000 cycles at 10 A g^{-1}, as shown in Figure S15. The results demonstrate durability rates of approximately 81%, 94%, and 93% for the Py-DPABT CMP, Py-DPABT CMP-500, and Py-DPABT CMP-700, respectively. The Coulombic efficiencies for Py-DPABT CMP, Py-DPABT CMP-500, and Py-DPABT CMP-700 are 96.57%, 98.1%, and 99%, respectively, after 5000 cycles (Figure S16). In this study, electrochemical impedance spectroscopy was used to investigate the interactions between the electrolyte and electrode over a given frequency range, utilizing a KOH solution as the electrolyte. The Nyquist plot's intersection with the real Z′ axis, shown in Figure S17a, represents the solution resistance (R_s), which arises from three primary sources: the resistivity of the active materials, the inherent resistivity of the electrolyte, and the ability to resist the conductive electrode material to the current collector.

Figure S17b presents the equivalent fitted circuit of both Py-DPABT CMP-500 and Py-DPABT CMP-700, where R_s, R_{ct}, CPE−EDL, CPE−P, and Z_w relate to series resistance as well as transfer of charge resistance, constant phase elements reflecting EDLC and pseudocapacitive behavior, and the Warburg impedance, respectively. The ohmic resistances of Py-DPABT CMP-500 and Py-DPABT CMP-700 were measured to be 8.46 and 14.84 Ω, while their charge transfer resistances were 37.84 and 3936 Ω (Table S2). Additionally, Figure S17c presents a Bode plot displaying the frequency-dependent magnitude of the impedance. The outcomes show a typical slope at low frequencies and barely any resistance at higher frequencies, demonstrating the strong capacitive capabilities of the electrode materials. Furthermore, Figure S17d illustrates the frequency-dependent phase angle of the electrodes. The knee frequencies, corresponding to a phase angle of −45°, where capacitive and resistive properties are balanced, were identified as 9.03 Hz for Py-DPABT CMP-500 and 798 Hz for Py-DPABT CMP-700. These knee frequencies are considered indicators of the materials' rate capability and

https://doi.org/10.1021/acsapm.5c00012
ACS Appl. Polym. Mater. 2025, 7, 3324−3336

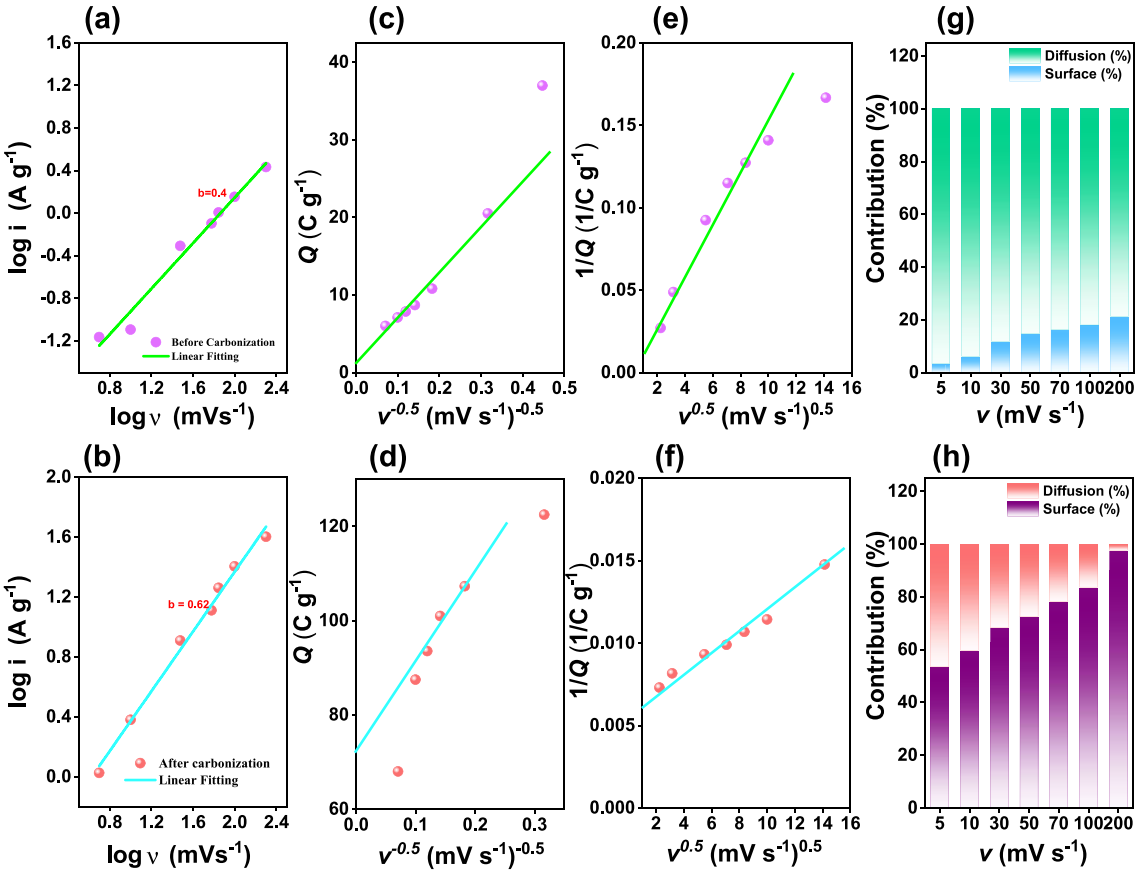

Figure 7. (a, b) The relation between peak current density and the square root of potential scan rate, (c, d) relation between Q (C g^{-1}) and $\nu^{-0.5}$ (mV s^{-1})$^{-0.5}$, (e, f) $1/Q$ vs $\nu^{0.5}$, and (h, g) percentage of surface contribution and diffusion-contribution for (a, c, e, g) Py-DPABT CMP and (b, d, f, h) Py-DPABT CMP-500.

display an adequate relationship. CV is considered a crucial method for analyzing a material's electrochemical behavior across a range of voltages, including its voltage process, reversible nature, and kinetics (whether diffusion or surface-controlled), as well as its energy storage mechanism. The electrochemical data were presented, followed by an analysis of the capacitive portion of the total charge storage. The charge-storing properties of the electrodes were examined using a power rule. This link between the utilized potential window (ν) and applied current density (i) is expressed by eq 1.

$$i(\mathrm{V}) = a\nu^{b} \text{ or } (\log i = a + b\log \nu) \tag{1}$$

The consistent parameters a and b are then established by examining the intercept as well as the incline of the (log i) against (log ν) plots. The value of b is determined by the incline calculated from the linear fit of the log i vs log ν plot at a constant voltage. A b value of 0.5 implies ion intercalation into the electrode, which is typical of a diffusion-controlled process, whereas a b value of 1 indicates capacitive behavior or control by nondiffusive mechanisms. As seen in Figure 7a,b, the plot between log i and log ν reveals a and b values of about 0.4, implying that ion intercalation is the major process for charge storage, as it is near to 0.5. Conversely, when the b value exceeds 0.5, it indicates that capacitive processes play a more significant role in the formation of the crystals than intercalation under those conditions. The Trasatti method is utilized to investigate the charge storage mechanisms in Py-DPABT CMP and Py-DPABT CMP-500 materials, determining the respective contributions of surface-controlled and nonsurface-controlled capacitive processes to total charge storage (Q_{total}).

The value of the outer charge (Q_{outer}), which peaks at the maximum potential scan rate and is predominantly a surface process, is illustrated in Figure 7c,d, which were determined using the specified eq 2.

$$Q = Q_{\text{outer}} + K\nu^{0.5} \tag{2}$$

The capacitance (C g^{-1}) obtained using cyclic voltammetry (CV) at corresponding potential sweep rates is represented by Q, whereas K is a constant and ν (mV s^{-1}) denotes the probable sweep value. To calculate the value of Q_{outer}, one can use the intercept from the plot of Q versus $\nu^{-0.5}$. Additionally, reduced scan rates allow ions more time to disperse, and under these conditions, the stored charges amount to the total charge (Q_{total}). For the materials Py-DPABT CMP and Py-DPABT CMP-500, shown in Figure 7c,d, the capacitance can be estimated using eq 3 based on the slope of ($1/Q$) and ($\nu^{0.5}$).

$$\frac{1}{Q} = \frac{1}{Q_{\text{total}}} + K\nu^{0.5} \tag{3}$$

Consequently, the Py-DPABT CMP and Py-DPABT CMP-500 electrodes display outer charges of 1.28 and 73.3 C g^{-1}, as well as with total charges of 101 and 169 C g^{-1} (Figure 7e,f). As a result, the diffusion-controlled faradic processes in Py-DPABT CMP account for 96.5% of the charge storage, while in Py-DPABT CMP-500, they contribute 46.5%. Figure 7g,h

https://doi.org/10.1021/acsapm.5c00012
ACS Appl. Polym. Mater. 2025, 7, 3324−3336

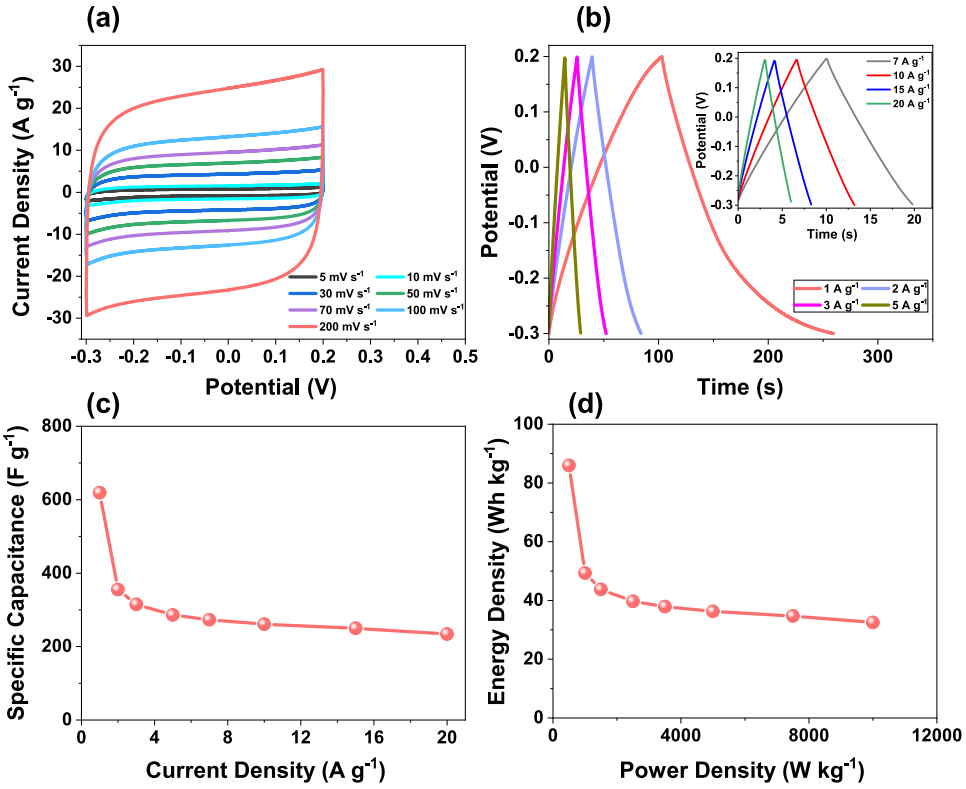

Figure 8. CV (a), GCD (b), specific capacitance (c), and Ragone (d) profiles for a symmetric supercapacitor coin cell of Py-DPABT CMP-500.

displays the proportions of diffusion-controlled and surface contributions across various applied scan speeds.

Constructing a Symmetric Supercapacitor Coin Cell for Py-DPABT CMP-500 and Py-DPABT CMP-700. Additionally, we employed a CR2032 coin cell to analyze the electrochemical properties of a symmetric supercapacitor using Py-DPABT CMP-500 and Py-DPABT CMP-700. As shown in Figures 8a and S18a, CV profiles were obtained at varying scan rates ranging from 5 to 200 mV s^{-1}. Due to EDLC and pseudocapacitive effects, the electrodes' curves had a virtually rectangular form with noticeable humps in the lower potential range, which is characteristic of supercapacitors.

The electrode had consistent durability as scan rates increased, reflecting higher current densities and enhanced performance and stability of the electrode materials. Additionally, Figures 8b and S18b illustrate GCD curves for Py-DPABT CMP-500 and Py-DPABT CMP-700, and GCD curves exhibited an almost triangular form with a noticeable bend, attributed to the heteroatoms in the material, which indicates the collective impacts of EDLC and pseudocapacitance. The specific capacitances of Py-DPABT CMP-500 and Py-DPABT CMP-700 achieved were 627 F g^{-1} and 121 F g^{-1} at 1 A g^{-1}, respectively (Figures 8c and S18c]. Compared with Py-DPABT CMP-700, Py-DPABT CMP-500 maintains a high level of 243 F g^{-1} even at 20 A g^{-1}, as shown in Figure 8c. As illustrated in Figures 8d and S18d, the Ragone plot indicates an energy density of 43.33 Wh kg^{-1} and 16.80 Wh kg^{-1} for Py-DPABT CMP-500 and Py-DPABT CMP-700, respectively. A cycle stability test of Py-DPABT CMP-500 and Py-DPABT CMP-700 was conducted over 5000 cycles, depicted in Figure S19, and demonstrated exceptional capacity retention of 99.55% and 98.51%, respectively. These results can be attributed to the heteroatoms enhancing the electrode–electrolyte interaction, which increased the surface area and facilitated the flow of electrolyte ions. The Coulombic efficiency for the symmetric supercapacitor coin cell of Py-DPABT CMP-500 is 98.9% after 5000 cycles (Figure S20). Additionally, the Nyquist plot for both Py-DPABT CMP-500 and Py-DPABT CMP-700 in a symmetric coin cell configuration was analyzed to evaluate key electrode properties, such as charge transfer resistance and series resistance, as shown in Figure S21a–d. In this setup, the initial series resistance (Ohmic resistance) obtained from Figure S21a was measured to be 16.95 Ω for Py-DPABT CMP-500 and 14.95 Ω for Py-DPABT CMP-700 (Table S2). In addition, the charge transfer resistances were recorded at 51.07 Ω and 68.76 Ω, respectively. This demonstrates the superior performance of the Py-DPABT CMP-500. The equivalent fitted circuit of both Py-DPABT CMP-500 and Py-DPABT CMP-700 was shown in Figure S21b, where R_s, R_{ct}, CPE–EDL, and Z_w correspond to the series resistance, charge transfer resistance, constant phase elements reflecting EDLC, and the Warburg impedance, respectively. Further, Figure S21c presents a Bode plot that illustrates the impedance magnitude as a function of frequency. The data reveal a typical slope at lower frequencies, with resistance decreasing as frequency increases, which indicates the electrode materials' strong capacitive behavior. Additionally, Figure S21d depicts the phase angle variation with frequency. The knee frequencies, where the phase angle reaches −45°, signifying a balance between capacitive and resistive characteristics, were determined to be 25.06 Hz for Py-DPABT CMP-500 and 81.94 Hz for Py-DPABT CMP-700. In terms of conductivity within the coin cell configuration, Py-DPABT CMP-500 demonstrated a value of 0.0195 S m^{-1}, compared to 0.0145 S m^{-1} for Py-DPABT CMP-700, indicating that Py-DPABT CMP-500 possesses superior

https://doi.org/10.1021/acsapm.5c00012
ACS Appl. Polym. Mater. 2025, 7, 3324–3336

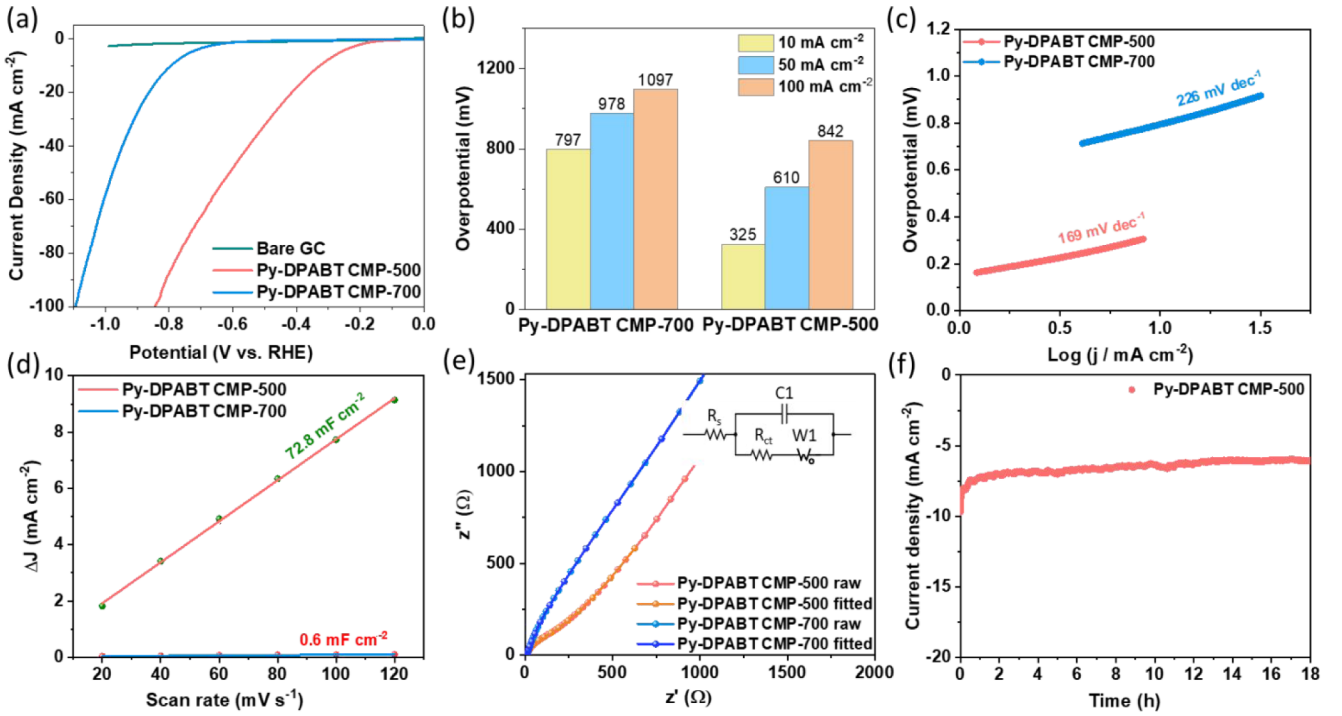

Figure 9. (a) LSV plots Bare GC, Py-DPABT CMP-500, and Py-DPABT CMP-500 in 1 M KOH electrolyte, (b) overpotential of different materials at different current densities, (c) Tafel slope of Py-DPABT CMP-500 and Py-DPA-BT-700, (d) capacitive current density as a function of scan rate, (e) Nyquist plots (inset shows the equivalent circuit diagram), and (f) chronoamperometry (*i-t*) plot of Py-DPABT CMP-500.

conductivity. Py-DPABT CMP-500 has lower resistance and higher conductivity, highlighting its abilities as a better substrate for electrodes for the storage of energy applications. Figure S22a illustrates the graph between log *i* and log *v* for the coin cell supercapacitor, showing a value of *b* close to 0.9, which approximates 1. This indicates that capacitive processes are more dominant than intercalation in this scenario. The coin cell supercapacitor possesses an outer charge of 22.8 C g^{-1} and a total charge of 37.8 C g^{-1} (Figures S22b and S22c). Figure S22d presents the percentage of diffusion-controlled and surface contributions across various applied scan speeds.

Electrochemical Hydrogen Production Performance of Py-DPABT CMP-500 and Py-DPABT CMP-700. The electrocatalytic HER activity of the synthesized samples was studied using a three-electrode system. Linear sweep voltammetry (LSV) measurements were carried out in a 1 M KOH solution, where a sharp increase in cathodic current indicated hydrogen generation via water splitting at specific negative potentials. As shown in Figure 9a, the carbonized samples demonstrated superior HER activity compared to the bare glassy carbon (GC) electrode. Notably, lower overpotential values were associated with enhanced electrocatalytic performance for HER. Py-DPABT CMP-500 required an overpotential of only 325 mV to achieve a current density of 10 mA cm^{-2}, significantly outperforming Py-DPABT CMP-700, which required 797 mV. This difference highlights the superior electrocatalytic efficiency of Py-DPABT CMP-500. Furthermore, the lower overpotentials required to reach higher current densities (50 and 100 mA cm^{-2}) for Py-DPABT CMP-500 further confirmed its promising HER activity (Figure 9b). The Tafel plots provided additional insights into the catalytic kinetics, as shown in Figure 9c. Py-DPABT CMP-500 exhibited a Tafel slope of 169 mV dec^{-1}, compared to 226 mV dec^{-1} for Py-DPABT CMP-700, indicating that Py-DPABT CMP-500 possessed faster reaction kinetics during the HER. C_{dl} is a key parameter for understanding the dual-layer behavior at the interface of the electrode−electrolyte. To determine C_{dl}, cyclic voltammograms (CVs) were taken in nonfaradaic regions at various scan rates, and the C_{dl} was calculated from the slope of the ΔJ versus scan rate plots. The CV profiles of the samples (Figure S23) exhibited a rectangular shape, indicative of the double-layer capacitance behavior of the catalysts. As shown in Figure 9d, Py-DPABT CMP-500 displayed an exceptionally high C_{dl} value of 72.8 mF cm^{-2}, which is approximately 121 times greater than that of Py-DPABT CMP-700 (0.6 mF cm^{-2}). In addition to LSV, Tafel slopes, and double-layer capacitance, the R_{ct} at the electrode−electrolyte interface, derived from Nyquist plots, provides valuable insights into electrocatalytic activity. As depicted in Figure 9e, Py-DPABT CMP-500 exhibited a significantly lower R_{ct} value of 88 Ω compared to 195 Ω for Py-DPABT CMP-700. This lower R_{ct} value indicates superior charge transfer capabilities at the interface of the electrode−electrolyte. The enhanced outcomes of Py-DPABT CMP-500 can be attributed to its high surface area and extended conjugated π-electronic structure, which provide a large electrode−electrolyte interfacial area and facilitate efficient charge transfer. A current−time (*i-t*) stability test was used to evaluate the catalysts' endurance over time. As shown in Figure 9f, Py-DPABT CMP-500 exhibited remarkable stability, maintaining a nearly constant current density at −0.32 V vs RHE over 18 h. This result underscores the excellent electrochemical stability of Py-DPABT CMP-500 for alkaline HER applications.

CONCLUSIONS

In summary, we developed N- and S-doped microporous carbons (Py-DPABT CMP-500) through a one-step carbonization process using Py-DPABT CMP as the atomic source at

https://doi.org/10.1021/acsapm.5c00012
ACS Appl. Polym. Mater. 2025, 7, 3324−3336

500 °C. These materials serve as excellent candidates for CO_2 capture and as organic electrodes in supercapacitors (SCs). The resulting Py-DPABT CMP-500 showed exceptional ability to SA_{BET} of 423 m^2 g^{-1} and CO_2 uptake up to 3.55 mmol g^{-1}. Doped with N and S heteroatoms, the material showed exceptional electrochemical properties, such as a specific capacitance of 973 F g^{-1}. The exceptional capacitance is attributable to its high SA_{BET}, and the occurrence of electrochemically active heteroatoms is retained after the carbonization process. In addition to CO_2 uptake and supercapacitor applications, the HER of Py-DPABT CMP-500 was investigated in a 1 M KOH electrolyte using a three-electrode system. The material achieved a current density of 10 mA cm^{-2} with an overpotential of 325 mV and exhibited a Tafel slope of 169 mV dec^{-1}. This study introduced a simple method for producing high-value carbon materials from CMP, examining their possible uses in HER applications, gas capture, and high-performance energy storage systems.

■ ASSOCIATED CONTENT

Supporting Information

The Supporting Information is available free of charge at https://pubs.acs.org/doi/10.1021/acsapm.5c00012.

Electrochemical measurements; spectroscopic data for Py-T, DPABT, and DPABT-Br_2; preparation of Py-DPABT CMP-500 and Py-DPABT CMP-700; XRD spectrum of Py-DPABT CMP; TGA and Ramman profiles of Py-DPABT CMP-500 and Py-DPABT CMP-700; XRD and XPS survey profiles of Py-DPABT CMP-500; BET data of Py-DPABT CMP-700; SEM and SEM-EDS images of Py-DPABT CMP, Py-DPABT CMP-500, and Py-DPABT CMP-700; electrochemical data including CV and GCD of Py-DPABT CMP-700; the columbic efficiency and stability profiles for Py-DPABT CMP, Py-DPABT CMP-500, and Py-DPABT CMP-700; EIS curves of Py-DPABT CMP-500 and Py-DPABT CMP-700 based on three-electrode system and symmetric coin cell; comparison between the specific surface area/specific capacitance of Py-DPABT CMP and Py-DPABT CMP-500 with those of previously reported materials for supercapacitor application and the EIS fitting data for Py-DPABT CMP-500 and Py-DPABT CMP-700 were obtained from both a three-electrode system and a symmetric coin cell setup (PDF)

■ AUTHOR INFORMATION

Corresponding Author

Shiao-Wei Kuo − *Department of Materials and Optoelectronic Science, College of Semiconductor and Advanced Technology Research, Center for Functional Polymers and Supramolecular Materials, National Sun Yat-Sen University, Kaohsiung 804, Taiwan; Department of Medicinal and Applied Chemistry, Kaohsiung Medical University, Kaohsiung 807, Taiwan;* orcid.org/0000-0002-4306-7171; Email: kuosw@faculty.nsysu.edu.tw

Authors

Poonam Nagendra Singh − *Department of Materials and Optoelectronic Science, College of Semiconductor and Advanced Technology Research, Center for Functional Polymers and Supramolecular Materials, National Sun Yat-Sen University, Kaohsiung 804, Taiwan*

Mohamed Gamal Mohamed − *Department of Materials and Optoelectronic Science, College of Semiconductor and Advanced Technology Research, Center for Functional Polymers and Supramolecular Materials, National Sun Yat-Sen University, Kaohsiung 804, Taiwan; Department of Chemistry, Faculty of Science, Assiut University, Assiut 71515, Egypt;* orcid.org/0000-0003-0301-8372

Mohammed G. Kotp − *Department of Materials and Optoelectronic Science, College of Semiconductor and Advanced Technology Research, Center for Functional Polymers and Supramolecular Materials, National Sun Yat-Sen University, Kaohsiung 804, Taiwan*

Tapomay Mondal − *Department of Materials and Optoelectronic Science, College of Semiconductor and Advanced Technology Research, Center for Functional Polymers and Supramolecular Materials, National Sun Yat-Sen University, Kaohsiung 804, Taiwan*

Swetha V. Chaganti − *Department of Chemistry, National Sun Yat-Sen University, Kaohsiung 80424, Taiwan*

Mervat Ibrahim − *Chemistry Department, Faculty of Science, New Valley University, El-Kharja 72511, Egypt*

Santosh U. Sharma − *Institute of Chemistry, Academia Sinica, Taipei 115, Taiwan*

Yunsheng Ye − *Department of Materials and Optoelectronic Science, College of Semiconductor and Advanced Technology Research, Center for Functional Polymers and Supramolecular Materials, National Sun Yat-Sen University, Kaohsiung 804, Taiwan*

Complete contact information is available at: https://pubs.acs.org/10.1021/acsapm.5c00012

Author Contributions

$^{\nabla}$P.N.S. and M.G.M. contributed equally to this work.

Notes

The authors declare no competing financial interest.

■ ACKNOWLEDGMENTS

This study was supported financially by the National Science and Technology Council, Taiwan, under contracts NSTC 113-2223-E-110-001 and 113-2218-E-110-004. The authors thank the staff at National Sun Yat-sen University for their assistance with the TEM (ID: EM022600) experiments.

■ REFERENCES

(1) Amrouche, S. O.; Rekioua, D.; Rekioua, T.; Bacha, S. Overview of energy storage in renewable energy systems. *Int. J. Hydrogen Energy* **2016**, *41* (48), 20914−20927.

(2) Mohamed, M. G.; Chang, W. C.; Chaganti, S. V.; Sharma, S. U.; Lee, J. T.; Kuo, S. W. Dispersion of ultrastable crown-ether-functionalized triphenylamine and pyrene-linked porous organic conjugated polymers with single-walled carbon nanotubes as high-performance electrodes for supercapacitors. *Polym. Chem.* **2023**, *14*, 4589−4601.

(3) Mohamed, M. G.; Sharma, S. U.; Wang, P. T.; Ibrahim, M.; Lin, M. H.; Liu, C. L.; Ejaz, M.; Yen, H. J.; Kuo, S. W. Construction of fully π-conjugated, diyne-linked conjugated microporous polymers based on tetraphenylethene and dibenzo[g,p]chrysene units for energy storage. *Polym. Chem.* **2024**, *15*, 2827−2839.

(4) Mohamed, M. G.; Chaganti, S. V.; Sharma, S. U.; Samy, M. M.; Ejaz, M.; Lee, J. T.; Zhang, K.; Kuo, S. W. Constructing Conjugated Microporous Polymers Containing the Pyrene-4,5,9,10-Tetraone Unit for Energy Storage. *ACS Appl. Energy Mater.* **2022**, *5*, 10130−10140.

(5) Sharma, S. U.; Elsayed, M. H.; Mekhemer, I. M. A.; Meng, T. S.; Chou, H. H.; Kuo, S. W.; Mohamed, M. G. Rational design of pyrene

and thienyltriazine-based conjugated microporous polymers for high-performance energy storage and visible-light photocatalytic hydrogen evolution from water. *Giant* **2024**, *17*, 100217.
(6) Septiani, N. L. W.; Kaneti, Y. V.; Fathoni, K. B.; Wang, J.; Ide, Y.; Yuliarto, B.; Nugraha; Dipojono, H. K.; Nanjundan, A. K.; Golberg, D.; Bando, Y.; Yamauchi, Y. Self-assembly of nickel phosphate-based nanotubes into two-dimensional crumpled sheet-like architectures for high-performance asymmetric supercapacitors. *Nano Energy* **2020**, *67*, 104270.
(7) Hu, X.; Luo, Y.; Wu, X.; Niu, J.; Tan, M.; Sun, Z.; Liu, W. Heteroatom-doped microporous carbon nanosheets derived from pentaerythritol-melamine for supercapacitors and CO_2 capture. *Mater. Today Energy* **2022**, *27*, 101010.
(8) Li, L.; Lu, F.; Xue, R.; Ma, B.; Li, Q.; Wu, N.; Liu, H.; Yao, W.; Guo, H.; Yang, W. Ultra stable triazine-based covalent organic framework with an interlayer hydrogen bonding for supercapacitor applications. *ACS Appl. Mater. Interfaces* **2019**, *11*, 26355−26363.
(9) Amin, K.; Ashraf, N.; Mao, L.; Faul, C. F. J.; Wei, Z. Conjugated microporous polymers for energy storage: Recent progress and challenges. *Nano Energy* **2021**, *85*, 105958.
(10) Xingang, L.; Li, Y.; Zeng, L.; Li, X.; Chen, N.; Bai, S.; He, H.; Wang, Q.; Zhang, C. A review on mechanochemistry: Approaching advanced energy materials with greener force. *Adv. Mater.* **2022**, *34* (46), 2108327.
(11) Mohamed, M. G.; Ahmed, M. M. M.; Du, W. T.; Kuo, S. W. Meso/Microporous Carbons from Conjugated Hyper-Crosslinked Polymers Based on Tetraphenylethene for High-Performance CO_2 Capture and Supercapacitor. *Molecules* **2021**, *26*, 738.
(12) Mohamed, M. G.; Mansoure, T. H.; Samy, M. M.; Takashi, Y.; Mohammed, A. A. K.; Ahamad, T.; Alshehri, S. M.; Kim, J.; Matsagar, B. M.; Wu, K. C. W.; Kuo, S. W. Ultrastable Conjugated Microporous Polymers Containing Benzobisthiadiazole and Pyrene Building Blocks for Energy Storage Applications. *Molecules* **2022**, *27*, 2025.
(13) Zhang, J.; Gu, M.; Chen, X. Supercapacitors for renewable energy applications: A review. *Micro. Nano. Energy* **2023**, *21*, 100229.
(14) Zheng, S.; Miao, L.; Sun, T.; Li, L.; Ma, T.; Bao, J.; Tao, Z.; Chen, J. An extended carbonyl-rich conjugated polymer cathode for high-capacity lithium-ion batteries. *J. Mater. Chem. A* **2021**, *9*, 2700−2705.
(15) Mohamed, M. G.; Chang, W. C.; Kuo, S. W. Crown Ether- and Benzoxazine-Linked Porous Organic Polymers Displaying Enhanced Metal Ion and CO_2 Capture through Solid-State Chemical Transformation. *Macromolecules* **2022**, *55*, 7879−7892.
(16) Ray, B.; Churipard, S. R.; Peter, S. C. An overview of the materials and methodologies for CO_2 capture under humid conditions. *J. Mater. Chem. A* **2021**, *9*, 26498−26527.
(17) Piacentini, R. D.; Mujumdar, A. S. Climate change and drying of agricultural products. Dry. *Technol* **2009**, *27*, 629−635.
(18) Wickramaratne, N. P.; Jaroniec, M. Tailoring microporosity and nitrogen content in carbons for achieving high uptake of CO_2 at ambient conditions. *Adsorption* **2014**, *20*, 287−293.
(19) Hanifa, M.; Agarwal, R.; Sharma, U.; Thapliyal, P. C.; Singh, L. P. A review on CO_2 capture and sequestration in the construction industry: Emerging approaches and commercialised technologies. *J. CO2 Util.* **2023**, *67*, 102292.
(20) Ding, M.; Liu, X.; Ma, P.; Yao, Y. Porous materials for capture and catalytic conversion of CO_2 at low concentration. *Coord. Chem. Rev.* **2022**, *465*, 214576.
(21) Zhang, T.; Xing, G.; Chen, W.; Chen, L. Porous organic polymers: a promising platform for efficient photocatalysis. *Mater. Chem. Front.* **2020**, *4*, 332−353.
(22) Kaur, P.; Hupp, J. T.; Nguyen, S. T. Porous organic polymers in catalysis: opportunities and challenges. *ACS Catal.* **2011**, *1*, 819−835.
(23) Hsiao, C. W.; Elewa, A. M.; Mohamed, M. G.; Kuo, S. W. Highly stable hybrid porous polymers containing polyhedral oligomeric silsesquioxane (POSS)/Dibenzo[g,p]chrysene and Dibenzo[b,d]thiophene units for efficient Rhodamine B dye removal. *Sep. Purif. Technol.* **2024**, *332*, 125771.
(24) He, W.; Duan, J.; Liu, H.; Qian, C.; Zhu, M.; Zhang, W.; Liao, Y. Conjugated microporous polymers for advanced chemical sensing applications. *Prog. Polym. Sci.* **2024**, *148*, 101770.
(25) Lin, M. H.; Mohamed, M. G.; Lin, C. J.; Sheng, Y. J.; Kuo, S. W.; Liu, C. L. Achieving High zT with Carbon Nanotube/Conjugated Microporous Polymer Thermoelectric Nanohybrids by Meticulous Molecular Geometry Design. *Adv. Funct. Mater.* **2024**, *34*, 2406165.
(26) Mohamed, M. G.; Elsayed, M. H.; Li, C. J.; Hassan, A. E.; Mekhemer, I. M. A.; Musa, A. F.; Hussien, M. K.; Chen, L. C.; Chen, K. H.; Chou, H. H.; Kuo, S. W. Reticular design and alkyne bridge engineering in donor−π−acceptor type conjugated microporous polymers for boosting photocatalytic hydrogen evolution. *J. Mater. Chem. A* **2024**, *12*, 7693−7710.
(27) Fischer, S.; Schimanowitz, A.; Dawson, R.; Senkovska, I.; Kaskel, S.; Thomas, A. Cationic microporous polymer networks by polymerisation of weakly coordinating cations with CO_2-storage ability. *J. Mater. Chem. A* **2014**, *2*, 11825−11829.
(28) Xu, Y.; Jin, S.; Xu, H.; Nagai, A.; Jiang, D. Conjugated microporous polymers: design, synthesis and application. *Chem. Soc. Rev.* **2013**, *42*, 8012−8031.
(29) Chaoui, N.; Trunk, M.; Dawson, R.; Schmidt, J.; Thomas, A. Trends and challenges for microporous polymers. *Chem. Soc. Rev.* **2017**, *46*, 3302−3321.
(30) Liao, Y.; Wang, H.; Zhu, M.; Thomas, A. Efficient supercapacitor energy storage using conjugated microporous polymer networks synthesized from Buchwald−Hartwig coupling. *Adv. Mater.* **2018**, *30*, 1705710.
(31) Lu, H.; Zhao, X. S. Biomass-derived carbon electrode materials for supercapacitors. *Sustain. Energy Fuels* **2017**, *1*, 1265−1281.
(32) Havinga, E. E.; Ten Hoeve, W.; Wynberg, J. P. B. A new class of small band gap organic polymer conductors. *Polym. Bull.* **1992**, *29*, 119−126.
(33) Gora, M.; Krzywiec, W.; Mieczkowski, J.; Maia, E. C. R.; Louarn, G.; Zagorska, M.; Pron, A. Alternating copolymers of diketopyrrolopyrrole or benzothiadiazole and alkoxy-substituted oligothiophenes: Spectroscopic, electrochemical and spectroelectrochemical investigations. *Electrochim. Acta* **2014**, *144*, 211−220.
(34) Parker, T. C.; Patel, D. G.; Moudgil, K.; Barlow, S.; Risko, C.; Brédas, J.-L.; R, J.; Reynolds, J. R.; Marder, S. R. Heteroannulated acceptors based on benzothiadiazole. *Mater. Horiz.* **2015**, *2* (1), 22−36.
(35) Neto, B. A. D.; Lapis, A. A. M.; Da Silva, E. N., Jr; Dupont, J. 2,1,3-Benzothiadiazole and Derivatives: Synthesis, Properties, Reactions, and Applications in Light Technology of Small Molecules. *Eur. J. Org. Chem.* **2013**, *2*, 228−255.
(36) Rakitin, O. A. Fused 1,2,5-thia-and 1,2,5-selenadiazoles: Synthesis and application in materials chemistry. *Tetrahedron Lett.* **2020**, *61*, 152230.
(37) Rakitin, O. A. Recent developments in the synthesis of 1,2,5-thiadiazoles and 2,1,3-benzothiadiazoles. *Synthesis* **2019**, *51*, 4338−4347.
(38) Kukhta, N. A.; Batsanov, A. S.; Bryce, M. R.; Monkman, A. P. Importance of chromophore rigidity on the efficiency of blue thermally activated delayed fluorescence emitters. *J. Phys. Chem. C* **2018**, *122*, 28564−28575.
(39) Pan, J. Q.; Yi, J. P.; Xie, G.; Lai, W. Y.; Huang, W. Enhancing optical gain stability for a deep-blue emitter enabled by a low-loss transparent matrix. *J. Phys. Chem. C* **2018**, *122*, 21569−21578.
(40) Mahesh, K.; Priyanka, V.; Vijai Anand, A. S.; Karpagam, S. Photophysical and electrochemical investigation of highly conjugated pyridine-based diphenylamine materials. *J. Mol. Struct.* **2018**, *1154*, 445−454.
(41) Hancharova, M.; Mazur, K.; Halicka, K.; Zając, D. Derivatives of diphenylamine and benzothiadiazole in optoelectronic applications: a review. *J. Polym. Res.* **2022**, *29*, 417.
(42) Li, J.; Xie, X.; Zhong, W.; Liu, Z.; Jiang, W.; Hu, G. Preparation of inexpensive S-doped porous carbons for high-performance supercapacitors. *Diamond Relat. Mater.* **2024**, *142*, 110856.

https://doi.org/10.1021/acsapm.5c00012
ACS Appl. Polym. Mater. 2025, 7, 3324−3336

(43) Ejaz, M.; Mohamed, M. G.; Chen, Y. T.; Zhang, K.; Kuo, S. W. Porous carbon materials augmented with heteroatoms derived from hyperbranched biobased benzoxazine resins for enhanced CO_2 adsorption and exceptional supercapacitor performance. *J. Energy Storage* **2024**, *78*, 110166.
(44) Mohamed, M. G.; Samy, M. M.; Mansour, T. H.; Li, C.-J.; Li, W.-C.; Chen, J.-H.; Zhang, K.; Kuo, S.-W. Microporous Carbon and Carbon/Metal Composite Materials Derived from Bio-Benzoxazine-Linked Precursor for CO_2 Capture and Energy Storage Applications. *Int. J. Mol. Sci.* **2022**, *23* (1), 347.
(45) Singh, P. N.; Mohamed, M. G.; Kuo, S. W. Systematic Design and Synthesis of Conjugated Microporous Polymers Containing Pyrene and Azobenzene Building Materials for High-Performance Energy Storage. *ACS Appl. Energy Mater.* **2023**, *6*, 11342−11351.
(46) Weng, T. H.; Mohamed, M. G.; Sharma, S. U.; Mekhemer, I. M. A.; Chou, H. H.; Kuo, S. W. Rationally Engineered Ultrastable Three-Dimensional (3D) Conjugated Microporous Polymers Containing Triptycene, Tetraphenylethene, and Benzothiadiazole Units as Exceptional High-Performance Organic Electrodes for Supercapacitors. *ACS Appl. Energy Mater.* **2023**, *6*, 9012−9024.
(47) Mohamed, M. G.; Chang, S. Y.; Ejaz, M.; Samy, M. M.; Mousa, A. O.; Kuo, S. W. Design and Synthesis of Bisulfone-Linked Two-Dimensional Conjugated Microporous Polymers for CO_2 adsorption and Energy Storage. *Molecules* **2023**, *28*, 3234.
(48) Mohamed, M. G.; Ebrahium, S. M.; Hammam, A. S.; Kuo, S. W.; Aly, K. I. Enhanced CO_2 capture in nitrogen-enriched microporous carbons derived from Polybenzoxazines containing azobenzene and carboxylic acid units. *J. Polym. Res.* **2020**, *27*, 197.
(49) Xu, X.; Sielicki, K.; Min, J.; Li, J.; Hao, C.; Wen, X.; Chen, X.; Mijowska, E. One-step converting biowaste wolfberry fruits into hierarchical porous carbon and its application for high-performance supercapacitors. *Renewable Energy* **2022**, *185*, 187−195.
(50) Li, G.; Li, Y.; Chen, X.; Hou, X.; Lin, H.; Jia, L. One step synthesis of N, P co-doped hierarchical porous carbon nanosheets derived from pomelo peel for high performance supercapacitors. *J. Colloid Interface Sci.* **2022**, *605*, 71−81.
(51) Gao, R.; He, H.; Bai, J.; Hao, L.; Shen, R.; Zhang, P.; Li, Y.; Li, X. Pyrene-benzothiadiazole-based polymer/CdS 2D/2D organic/inorganic hybrid S-scheme heterojunction for efficient photocatalytic H_2 evolution. *Chin. J. Struc. Chem.* **2022**, *41*, 2206031−2206038.
(52) Gu, S.; He, J.; Zhu, Y.; Wang, Z.; Chen, D.; Yu, G.; Pan, C.; Guan, J.; Tao, K. Facile carbonization of microporous organic polymers into hierarchically porous carbons targeted for effective CO_2 uptake at low pressures. *ACS Applied Mater. Interfaces* **2016**, *28*, 18383−18392.
(53) Singh, R.; Wang, L.; Ostrikov, K. J.; Huang, J. Designing Carbon-Based Porous Materials for Carbon Dioxide Capture. *Adv. Mater. Interfaces* **2024**, *11*, 2202290.
(54) Wu, P.; Wang, Y.; Liu, Y. Recent advances in heteroatom-doped porous carbon for adsorption of gaseous pollutants. *Chem. Eng. J.* **2024**, *491*, 152142.
(55) Saha, D.; Kienbaum, M. J. Role of oxygen, nitrogen and sulfur functionalities on the surface of nanoporous carbons in CO_2 adsorption: a critical review. *Microporous Mesoporous Mater.* **2019**, *287*, 29−55.
(56) Mohamed, M. G.; Chen, C.-C.; Ibrahim, M.; Mousa, A. O.; Elsayed, M. H.; Ye, Y.; Kuo, S.-W. Tetraphenylanthraquinone and Dihydroxybenzene-Tethered Conjugated Microporous Polymer for Enhanced CO_2 Uptake and Supercapacitive Energy Storage. *JACS Au.* **2024**, *4* (9), 3593−3605.
(57) Basit, A.; Mohamed, M. G.; Ejaz, M.; Su, B. X.; Manzoor, H.; Kuo, S.-W. Boosting Supercapacitor Energy Storage Using Microporous Carbon Derived from an Octavinylsilsesquioxane and Fluorenone-Linked Porous Hybrid Polymer. *ACS Appl. Energy Mater.* **2024**, *7* (17), 7505−7516.
(58) Basit, A.; Mohamed, M. G.; Sharma, S. U.; Kuo, S. W. Thianthrene- and Thianthrene Tetraoxide-Functionalized Conjugated Microporous Polymers for Efficient Energy Storage. *ACS Appl. Polym. Mater.* **2024**, *6*, 12247−12260.
(59) Basit, A.; Kao, Y. C.; El-Ossaily, Y.; Kuo, S. W.; Mohamed, M. G. Rational Engineering and Synthesis of Pyrene and Thiazolo[5,4-d]thiazole-Functionalized Conjugated Microporous Polymers for Efficient Supercapacitor Energy Storage. *J. Mater. Chem. A* **2024**, *12*, 30508−30521.
(60) Mohamed, M. G.; Sharma, S. U.; Liu, N.-Y.; Mansour, T. H.; Samy, M. M.; Chaganti, S. V.; Chang, Y.-L.; Lee, J.-T.; Kuo, S.-W. Ultrastable Covalent Triazine Organic Framework Based on Anthracene Moiety as Platform for High-Performance Carbon Dioxide Adsorption and Supercapacitors. *Int. J. Mol. Sci.* **2022**, *23* (6), 3174.
(61) Samy, M. M.; Mohamed, M. G.; Kuo, S. W. Directly synthesized nitrogen-and-oxygen−doped microporous carbons derived from a bio-derived polybenzoxazine exhibiting high-performance supercapacitance and CO_2 uptake. *Eur. Polym. J.* **2020**, *138*, 109954.
(62) Zhai, S.; Li, K.; Li, C.; Zhai, C.; Han, Q.; Zhang, Z.; Fu, Y.; Li, X.; Jin, K.; Cai, Z.; Zhao, Y. Lignin-derived N,S-codoped hierarchical porous carbons with high mesoporous rate for sustainable supercapacitive energy storage. *J. Energy Storage* **2024**, *85*, 111036.
(63) Mohamed, M. G.; Kotp, M. G.; Mousa, A. O.; Li, Y.-S.; Kuo, S.-W. Construction of Fe- and N-Doped Microporous Carbon from Ferrocene-Based Conjugated Microporous Polymers for Supercapacitive Energy Storage. *ACS Appl. Energy Mater.* **2025**.
(64) Mohamed, M. G.; Su, B. X.; Kuo, S. W. Robust Nitrogen-Doped Microporous Carbon via Crown Ether-Functionalized Benzoxazine-Linked Porous Organic Polymers for Enhanced CO_2 Adsorption and Supercapacitor Applications. *ACS Appl. Mater. Interfaces* **2024**, *16*, 40858−40872.
(65) Chaganti, S. V.; Sharma, S. U.; Ibrahim, M.; Basit, A.; Singh, P. N.; Kuo, S. W.; Mohamed, M. G. Redox-active a pyrene-4,5,9,10-tetraone and thienyltriazine-based conjugated microporous polymers for boosting faradaic supercapacitor energy storage. *J. Power Sources* **2025**, *627*, 235848.
(66) Lin, M. C.; Kuo, S. W.; Mohamed, M. G. High-performance anthracene-linked covalent triazine frameworks with dual functions for CO_2 capture and supercapacitor applications. *Mater. Adv.* **2024**, *5*, 6222−6233.

https://doi.org/10.1021/acsapm.5c00012
ACS Appl. Polym. Mater. 2025, 7, 3324−3336